KSME

Springer

Journal of Mechanical Science and Technology 35 (11) 2021

Original Article
DOI 10.1007/s12206-021-1015-0

Keywords:
· High cycle fatigue
· Very high cycle fatigue
· High strength steel
· Shot peening
· Rotary bending fatigue test

Correspondence to:
Nak-Sam Choi
nschoi@hanyang.ac.kr

Citation:
Myung, N., Wang, L., Choi, N.-S. (2021). High-cycle and very high-cycle bending fatigue strength of shot peened spring steel. Journal of Mechanical Science and Technology 35 (11) (2021) 4963~4973. http://doi.org/10.1007/s12206-021-1015-0

Received May 6th, 2021
Revised July 1st, 2021
Accepted July 15th, 2021

† Recommended by Editor Chongdu Cho

High-cycle and very high-cycle bending fatigue strength of shot peened spring steel

NohJun Myung[1], Liang Wang[2] and Nak-Sam Choi[3]

[1]Department of Mechanical Engineering, Graduate School, Hanyang University, Seoul 04763, Korea, [2]Department of Mechanical Design Engineering, Graduate School, Hanyang University, Seoul 04763, Korea, [3]Department of Mechanical Engineering, Hanyang University, Ansan-si 15588, Korea

Abstract This paper examined bending fatigue strength of shot-peened spring steel under the high cycle fatigue (HCF) and very high cycle fatigue (VHCF), and analyzed the effects of shot-peening on the high strength spring steel through service life. Hourglass shape specimens made of spring steel (Si-Cr alloys) were prepared for the rotary bending fatigue test. Actual local stresses were quantitatively calculated to compensate for the applied stress amplitudes, through which it was clarified that the shot-peening had strongly positive effects on the HCF strength, but rather negative effect on the VHCF strength. The fracturing process examination confirmed that most fish-eye fractures arose at sites deeper than the compressive residual stress zone, which did not prevent the creation of the fish-eye. The fatigue strength improvement in the VHCF range was scarcely expected as a result of the shot-peening treatment.

1. Introduction

Long-life safety of transportation machine and energy industry structures has been concerned in recent years. Many researchers have studied the fatigue behavior of materials in the high cycle range of more than 10^7 cycles for high safety and reliability of engineering structural components such as turbine blades, bearings, and springs. Researchers have reported that the fatigue strength of high strength steel showed duplex S-N curves depending on the characteristics of fatigue failure. As the scope of fatigue test cycle (N_f) was expanded, the range of more than 10^7 cycles was classified as very high cycle fatigue (VHCF) [1-5]. Especially mechanical components such as springs and bearings used in transportation machine systems have usually experienced the VHCF stresses. However, in a common test level it takes a really long time to observe VHCF behavior. Various fatigue test methods have been implemented to solve this problem, including a cantilever type rotary bending fatigue tester used together with the ultrasonic-fatigue-test (UFT) employing ultrasonic resonance [3, 6-8]. Spring steels are very usually used in combustion motor valves and clutching or injection systems. They are typically subjected to cycling conditions beyond the fatigue limit condition of 10^7 cycles. Various spring steels (Si-Cr and Cr-V alloys) have been studied under the VHCF [3, 6-12].

Furuya et al. [3] reported the fatigue data of 10^{10} cycles for spring steel and discussed the size and frequency effects on the VHCF behavior. The fatigue strength at $N_f \cong 10^{10}$ cycles was lower than that at 10^8 cycles. The frequencies were fixed at 30 and 100 Hz with a multiple rotating bending machine, 120 Hz with an electromagnetic machine, 600 Hz with a high-speed servo-hydraulic machine, and 20 kHz with an ultrasonic machine. The frequency dependency was very small to obtain appropriate fatigue results. Bathias et al. [6] performed fatigue tests on various metal materials. The fatigue tests were performed at 20 kHz with a stress ratio ($R = \sigma_{min}/\sigma_{max}$) R = -1 under load control. Fatigue test results of spring steel (Cr-V, Cr-Si) showed that fatigue failure occurred in the VHCF range, and the fatigue strength decreased. Pyttel et al. [10] studied VHCF tests on helical compression springs made of SiCr- and SiCrV-alloys with

shot-peening treatment. There was no fatigue limit, but a remarkable decrease of fatigue strength in the N_f range of 10^7~1.5×10^9 cycles.

Murakami et al. [13, 14] studied influential factors in metal fatigue and reported that fatigue strength was significantly affected by crack initiation sites (surface or interior). Based on scanning electron microscope (SEM) fractography, Nishijima et al. [15] reported multiple fish-eye regions on a single fracture surface. Micro-cracks caused by a nonmetallic inclusion or hardened site inside the specimen skin were formed simultaneously at multiple sites due to stress concentration. However, the most critical crack was present in the skin and caused fracture initiation. In the fish-eye region, granular-bright facets (GBFs) were observed. Micro-cracking was mainly caused by stress concentration at the crack tip or inclusion boundary in GBF. The fatigue strength corresponding to the internal fracture initiation should be much higher than that to the surface fracture initiation, because the interior suffers lower local stresses than the surface at the same load level [16-19].

There are various methods for improving the fatigue strength of metals. Shot-peening treatment [20-25] is one of the effective methods for improving the fatigue strength of high strength steels [9, 26-30]. Fargas et al. [30] studied the relationship between microstructural changes induced by shot-peening and high cycle fatigue (HCF) limit ($N_f < 10^6$ cycles) using the staircase method. The fatigue tester was under load control in a resonant testing machine (150 Hz, R = 0.1). For fully annealed austenitic steel, even lower fatigue limits were obtained after shot-peening, because of high roughness generated by shot-peening. Li et al. [31] also predicted a decrease in fatigue limit on the basis of stress concentration effect induced by the increase of surface roughness formed due to shot-peening. However for cold rolled steel which is a mixture of austenite and martensite, the fatigue limit was improved by shot-peening for cycles lower than 106 [30]. Bagherifard et al. [32] reported that notched specimens of 39NiCrMo3 steel showed fatigue strength improvement for severely shot peened specimens in spite of their very high surface roughness: fatigue limit at run-out of 3×10^6 cycles increased by 12~33 % with peening coverage 100 %, and drastically increased by 146 % with 1500 % coverage.

In a study that extended the N_f over the giga-cycle range, Shiozawa et al. [2] reported the shot-peening effects of obstructing the crack initiation and propagation in high carbon chromium steel. Lee et al. [29] performed the cantilever type fatigue test over giga-cycles using shot-peened steels, which were classified according to different kinds of shot-peening conditions. For shot peened high strength quenched and tempered 50CrMo4 steel according to DIN EN 10083-3, Trško et al. [33] reported a significant increase of fatigue strength in the VHCF regime of ultrasonic fatigue testing at a frequency of 20 kHz. Benedetti et al. [34] studied the VHCF behaviors of shot-peened aluminum alloy plates considering the variation of residual stress and surface state by analyzing fatigue crack occurrence and propagation. Most studies above suggest that shot-peening can help improve the fatigue strength. However considerable ambiguity in mechanical and microstructural aspects still remains to clarify consistently the effects of shot peening on the fatigue strength in the VHCF range for high strength steels.

In this study, shot-peening effects on the VHCF strength as well as the HCF strength are examined through the rotary bending fatigue test of commercially available spring steel (Si-Cr-Mn alloy, SAE9254). The compressive residual stress in the skin, the surface roughness, and the microstructure change generated by shot-peening are reflected quantitatively in the actual stress amplitude calculation. The VHCF behaviors in improving the fatigue limit are re-analyzed through actual stress calculation based on the inclusion location and the fish-eye growth characteristics in the fracture initiation.

Table 1. Chemical composition of SAE9254 (wt.%). This material is hot-rolled spring steel of Si-Cr-Mn alloy, which has been widely used also as a commercial code of SPS 8.

C	Si	Mn	P	S	Cr
0.51	1.20~1.60	0.60~0.90	≤0.035	≤0.035	0.60~0.90

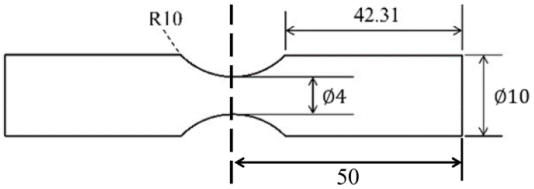

Fig. 1. Geometry of a rotary bending fatigue specimen used in this study (mm). The gauge portion is shaped with a diameter of 10 mm where the nominal stress at the central surface of the specimen is compensated with the concentration factor of 1.08 which was offered by the manufacturer of the tester.

2. Experimental procedure

2.1 Spring steel specimen and shot-peening treatment

The material used in this study was hot-rolled spring steel (Si-Cr-Mn alloys, SPS 8, SAE9254), which is used for high corrosion resistant spring components in vehicle engines. The chemical composition is shown in Table 1. The rotary bending fatigue specimens were prepared as in the hourglass shape of Fig. 1. Round bar specimens for tensile test were prepared per ASTM E8 standards.

The specimens were immersed in a furnace at 830 °C for 90 min and then quenched in oil. Subsequently, they were tempered at 400 °C for 120 min, and then air-cooled. Through this heat treatment, the surface hardness of the skin was increased to above that of HB390 to meet the criteria of spring steel SAE9254. The surface was polished with sandpaper (# 2000) to remove surface contaminations. A shot-peening treatment was then applied to the specimens employing an impeller type

shot-peening machine with an impeller diameter of 360 mm. Shot steel balls with a diameter of 300 μm impacted against the whole surface of round bar specimens during their rotation for 6 min so that a representative 200 % surface coverage [23] was achieved for usual industry application. The angle of impingement on the target surface was almost at right angles.

2.2 Residual stress and surface roughness measurement

For measurement of residual stress and surface roughness the above hot-rolled spring steel was sectioned into a plate type specimen, and processed under the same heat treatment and shot-peening conditions as the fatigue test specimens. The surface roughness of the specimen was measured with a non-contact roughness meter (Nano scan E1000) to examine changes in surface roughness due to shot-peening. The measuring area was set to 1000 μm× 1000 μm. An X-ray beam stress measurement tester (Rigaku MSF/PSF-3M) was used to measure the residual stress, and the volume ratio of austenite microstructure. The residual stresses were measured based on a linear plot of X-ray diffraction (XRD) data using the sin2ψ method of measuring the interplanar distance of the changed crystals. Exposure conditions for XRD are shown in Table 2. The diffraction plane for residual stress measurement was set in the rolling direction <100> which was parallel to the specimen length. Residual stresses at the material surface (depth = 0) formed by electro-polishing were measured so that the scattering of X-rays was minimized. After each very shallow electro-polishing step, the residual stress measurement was conducted at the removed depth. The depth dimension was adjusted by controlling the electro-polishing time. After the residual stress test, the actual depth was measured using the non-contact roughness meter.

2.3 Tensile test and rotary bending fatigue test

The tensile properties of the specimens (ASTM E8) were measured with a displacement rate of 1 mm/min using a tensile tester (Instron 8516). The tensile test was performed for five specimens at each condition. The strain was measured by attaching an extensometer (Instron 3542).

A cantilever type rotary bending fatigue tester (YRB-200, Yamanoto) with four axis spindles was used for the fatigue test. At room temperature, the stress ratio (R) was maintained at -1, and the rotating speed was 3600 rpm. The nominal stress of the gauge portion was calculated basically conforming to the KS B ISO 1143 standards [35] given by the equation

$$\sigma = \alpha \frac{Mc}{I} \tag{1}$$

where M is the maximum bending moment (= P×m/2), c the distance from the neutral axis to a designated height in the specimen, I the geometrical moment of inertia at the gage part (= $\pi d^4/64$), α the stress concentration factor (1.08) offered by the manufacturer of the tester. P, m and d are the load, the fixed test span (40.5 mm) and the gage part cross-section diameter (4 mm) of the specimen, respectively. The stress amplitude was adopted to be ten constant load levels lower than the ultimate strength measured in the tensile test. The fatigue test limitation was set up to 2.5 × 10^8 cycles to cover the VHCF range.

Table 2. Experimental conditions for X-ray diffraction test. The test was conducted on a plate type specimen which had been processed with the same heat treatment and shot-peening as the fatigue test specimen.

Characteristic X-ray	K alpha
Tube type	Cr
Tube voltage	30 kV
Tube current	10 mA
Scan range	148-164 deg
Ψ (psi) angle	0, 18.4, 26.6, 33.2, 39.2, 45
Measurement area	ϕ 2 mm

2.4 Microscopic observation

Specimens were cut in the direction of the shot-peening perpendicular to the surface, and the cross-section surface was then polished and etched with 3 % nital solution. To investigate the microstructural factors that affect fatigue failure, the etched section and fatigue fracture surface were analyzed with an SEM (Mira3, Tescan) and energy dispersive X-ray spectroscopy (EDX, Mira3, Tescan).

3. Results and discussion

3.1 Residual stress and surface roughness variation formed by shot-peening

Fig. 2 shows the XRD measurement result of residual normal stress according to depths from the surface. Taking into account the stress redistribution caused by the electro-polished skin, measured residual stresses were corrected for material removal in accordance with Moored and Evans correction [36]. Correction amount was varied according to depths, and the maximum correction for shot-peened specimen was calculated to be about +12.1 MPa at the depth of 75 m. For unpeened specimen correction was small: +3.2 MPa in the maximum at depth 90 m. Specimens before shot-peening showed compressive residual stress of -190 MPa at approximately 10 μm depth. The compressive residual stress decreased rapidly at further depths, then vanished at a depth of 40 μm. With deeper depths, tensile residual stress appeared with only a small intensity. In contrast, the shot-peened specimen had a large compressive residual stress over a depth of 170 μm from the surface. The surface had compressive residual stress of about 350 MPa. The maximum compressive residual stresses of up to 480 MPa were formed with depth over 10 to 70 μm. Above

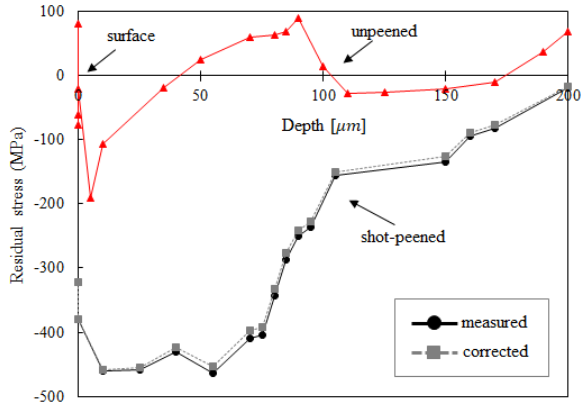

Fig. 2. Residual normal stress distributions measured along the depth from the specimen surface before and after the shot-peening. Stress redistribution induced by material removal of the electro-polished skin is reflected on the residual stresses, which is calculated in accordance with Moored and Evans correction [35].

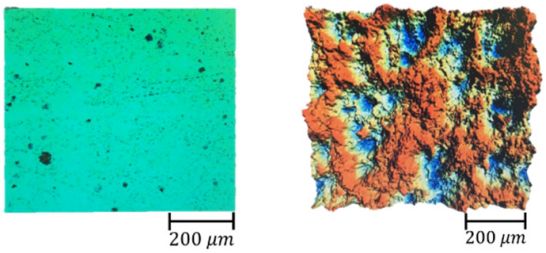

(a) (b)

Fig. 3. Surface roughness contours on the specimen surface measured with a non-contact roughness meter (Nano scan E1000): (a) unpeened; (b) shot-peened. Roughness data measured on the surface are displayed in Table 3.

the depth of 100 μm, the residual stress rapidly decreased and disappeared around the depth of 200 μm. Results of Wu et al. [21] using 18CrNiMo1.6 steel experienced with peening coverages 100~400 % showed maximum compressive stress distributions over depths of 50~75 μm, but had little effect of peening coverages on their maximum compressive residual stresses and their affected skin layer thicknesses. It was also confirmed in this experiment that the shot-peening generated large compressive residual stresses in such thin skin region of the specimens.

Fig. 3 shows contour images of the surface roughness in 800 × 800 μm^2 area before and after shot-peening. Table 3 shows average roughness (R_a) values representing the surface micro-profile height, and its root mean square (R_q), which is the standard deviation of the height distribution in the uneven portion. Ra increased by a factor of approximately 10 after shot-peening, and R_q also increased significantly. Due to the shot-peening treatment, the surface roughness became large over the entire specimen surface. The surface topography would change with initial surface treatments [21, 22], peening velocity and times [20-25].

Table 3. Surface roughness results represented by Ra and Rq values. Average roughness (R_a) represents the average micro-profile height, and its root mean square (R_q) indicates the standard deviation of the height distribution in the uneven portion.

	Roughness average (R_a, μm)	Root mean square (R_q, μm)
Unpeened	0.140	0.281
Shot-peened	1.411	1.708

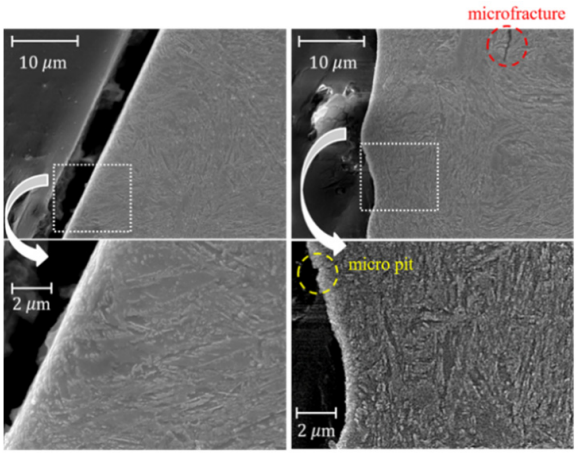

(a) (b)

Fig. 4. Microstructures of the sectioned skin part observed by SEM: (a) unpeened; (b) shot-peened. The shot-peening treatment definitely formed concave dimples approximately 3 μm deep from the surface. The microstructure of the skin part was crushed with the extremely compressive plastic deformation.

3.2 Microstructural change by shot-peening

Fig. 4 shows SEM images of the microstructure of skin parts for unpeened and shot-peened specimens. The shot-peening treatment formed dimples approximately 3 μm deep on the specimen surface. Microstructures of the skin part were observed to be crushed by the extremely compressive plastic deformation. A micro pit was occasionally generated on the surface (Fig. 4(b)), which seemed to originate from some surface defect or pull-out of inclusion in the sub-surface part and might suffer from local plastic deformation by the tangential tension along the contact surface boundary of an impactive shot steel ball during the compressive indentation [37]. The skin part was partially micro-cracked due to substantial plastic deformation (Fig. 4(b)), and thus the compressive residual stress would be relatively relaxed. As shown in Fig. 5, the length direction of crystal grains was observed rather horizontally for the skin up to approximately 20 μm depths underneath the surface. The severely deformed skin layer was similar to the results from high strength 50CrMo4 steel by Trško et al. [33] in which the thickness of the severely deformed skin layer was about 20 μm in terms of grain refinement microstructural change. Such shifted orientation of grains relatively parallel with the direction of the compressive residual normal stress (Fig. 2) would hinder crack propagation to the grain boundary,

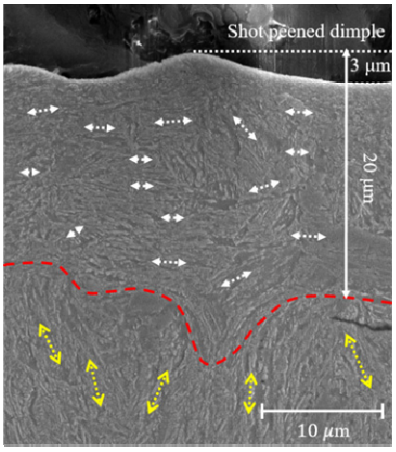

Fig. 5. Microstructural changes and plastic deformation according to depths after shot-peening. The length direction of crystal grains was shifted rather horizontally in the skin up to about 20 μm depths beneath the surface.

and increase fatigue life [17, 38]. For depths beyond 20 μm, grains remained in the original states shaped like the microstructure of unpeened specimens. Although the maximum compressive residual stresses were distributed at between 30 and 70 μm (Fig. 2), plastic deformation was hardly formed for the crystal grains. There were shown little changes in the shape of the fine grains, and the amount of austenite phase confirmed by EDX.

3.3 Stress concentration behaviors of the shot-peened skin part

For simulating the stress concentration behavior according to changes in surface roughness after shot-peening, stress concentration coefficients in various methods were calculated. Fig. 6 and Table 4 show the stress concentration factor K_{tn} according to the load and specimen type. The depth and radius of the dimples formed along the surface due to compressive indentation by shot-peening were measured with a sectioned specimen by SEM (Sec. 3.2), and are applied to the stress concentration equation. The measured dimple radius and depth were 15~30 μm and 3~7 μm, respectively. Based on the measured dimple data the maximum and minimum values in K_{tn} were calculated. The stress concentration factor in the present study for cases (b), (c) and (d) was calculated to be between 1.84 and 2.14, which is similar to the range observed in case (a) [13], in which the stress concentration behavior according to surface roughness was studied in the rotary bending fatigue test. The case (d) was also calculated, taking into account the micro pit and the micro fracture of Fig. 4(b). The depth and radius of the micro pit were about 0.2-0.3 μm, so small that the stress concentration effect seemed difficult to occur because a micro pit smaller than the grain size was reported not to affect the stress concentration [39-42]. The average of the stress concentration factor for the most common shot-peening notch shape was calculated to be $K_{tn} \cong 2.0$.

Table 4. Calculated values of stress concentration factors according to various loading and specimen types. The dimple radius and depth measured on the roughness profiles of Figs. 3 and 4 are applied to the equations in Fig. 6. Based on the measured dimple data the maximum and minimum values in K_{tn} are calculated.

	Specimen type	Load type	Stress concentration factor, K_{tn}	Reference
Case (a)	Cylinder	Rotary bending fatigue machine	1.842 (750 MPa) - 2.333 (950 MPa)	Murakami [13]
Case (b)	Plate	Tension	1.894~1.966	[43]
Case (c)	Plate	Tension	1.859~1.931	Cole and Brown [43]
Case (d)	Plate	Tension	1.936~2.140	Nishitani and Tada [44]

Table 5. Tensile properties of Si-Cr-Mn alloy before and after shot-peening (average ± standard deviation).

	Tensile strength (MPa)	Young's modulus (GPa)	Strain at break (%)
Unpeened	1604 ± 8.9	209 ± 4.8	12.0 ± 1.2
Shot-peened	1586 ± 0.9	210 ± 1.0	11.4 ± 0.5

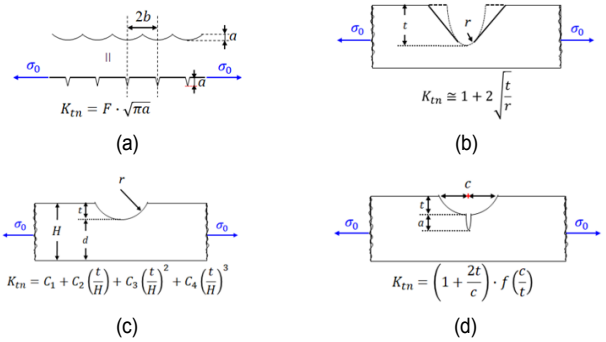

Fig. 6. Stress concentration factors (K_{tn}) according to the specimen surface profiles: (a) a periodic surface roughness; (b) an equivalent ellipse concept of a flat tension bar with a notch; (c) a flat tension bar with a U-shaped notch at one side; (d) a flat tension bar with double notch at one side. σ_0 indicates the nominal stress applied at the skin part. Those models of (a) to (d) may apply to the stress concentration circumstances at the shot-peened surface. Calculated values of K_{tn} are displayed in Table 4.

3.4 Shot-peening effects on tensile properties

Table 5 shows test data of tensile strength, Young's modulus, and strain at break measured from the specimens before and after shot-peening treatment. The tensile property values were represented by average ± standard deviation, which were calculated from the test data measured for five specimens.

After shot-peening, the tensile strength of spring steel decreased by approximately 1.1 % (18 MPa), Young's modulus hardly changed, and the strain at the break slightly diminished. The standard deviation of the data was very significantly reduced.

3.5 Shot-peening effects on fatigue test results

Fig. 7 shows the experimental data points of stress amplitude (σ_a) versus the number of fatigue test cycles (N_f) for unpeened and shot-peened specimens. The stair-case method was used to determine the fatigue limit: the upper stress level of 820 MPa was tested first, and then each stress amplitude was tested with a decrease by an interval of 5 MPa until the lower level of 785 MPa. At each stress level the fatigue test was conducted two times. If a specimen did not show a fracture until N_f reached 2.5×10^8, the fatigue test was stopped, and the specimen was marked as a run-out datum. Based on the test data, an S-N curve was derived that included the VHCF range. In the intermediate and high cycle range below 10^6 cycles, the unpeened specimens show a fatigue strength obviously lower than that for shot-peened specimens. The fatigue life of shot-peened specimens at each stress level was much longer than that of unpeened specimens. Several researchers [10, 27-29] have confirmed the improved fatigue strength of shot-peened specimens in the HCF range ($10^4 < N_f < 10^7$). However, in the VHCF range with N_f beyond 1.0×10^7 cycles, fatigue strengths of shot-peened specimens became lower than those of unpeened specimens. The shot-peening treatment would adversely affect the fatigue strength. For the HCF and VHCF ranges the corresponding S-N curve can be represented by a regression curve given in equation,

$$\sigma_a = \mathrm{A} - \mathrm{B}\cdot\log_{10} N_f \,. \tag{2}$$

Here, A is the y-intercept that indicates the initial fatigue strength and B represents the decreasing slope of fatigue strength as the life cycle increases. It is to be noted that the Eq. (2) adopts arithmetic σ_a versus logarithmic N_f. This may be more reasonable than a log-log relationship of σ_a and N_f in that the arithmetic scale of σ_a can represent accurate behaviors of the fatigue limit calculated in the VHCF range. The HCF and VHCF limit stresses were calculated through MINITAB on the basis of test data obtained by the staircase method. Based on the HCF range ($N_f \le 1.0\times10^7$), the fatigue limit (σ_f) of the unpeened and shot-peened specimens was 807.5 MPa and 815 MPa, respectively. Such values of σ_f were about 50.3 % and 51.4 % of the corresponding tensile strengths (σ_u) in Table 5, respectively, which were still about 2.5 times larger than the maximum allowable engineering stress (320 MPa) of the spring steel calculated assuming the safety factor of 5.0 for spring components.

Assuming that the fatigue limit of unpeened specimen was the same as that obtained from a uniaxial cyclic test, the following Goodman relation between σ_a and $\sigma_m+\sigma_{rd}$ may be considered to deduce a fatigue limit value for shot-peened specimen:

$$\frac{\sigma_a}{\sigma_{f0}} + \frac{\sigma_m + \sigma_{rd}}{\sigma_{u0}} = 1 \tag{3}$$

where σ_{f0} and σ_{u0} are the fatigue limit and the tensile strength of unpeened uniaxial specimen, respectively. The mean stress σ_m at any position in the specimen is zero for the rotary bending cyclic test. σ_{rd} is the maximum residual stress in Fig. 2. In Eq. (3) the stress amplitude σ_a can arrive at a fatigue limit which is expected by assuming a uniaxial specimen containing the pre-existent residual stresses. Thus expected fatigue limit values at $N_f = 1.0\times10^7$ are calculated to be 904.4 MPa (56.4 % σ_u) and 1059.5 MPa (66.8 % σ_u) for unpeened and shot peened specimens, respectively. However, the expected limits were considerably larger than those measured experimentally by the staircase method. Such difference for unpeened specimen may be caused by specimen types of uniaxial test and the present rotary bending test, and it for shot-peened specimen may originate from residual stress distribution characteristics and microstructural changes in addition to specimen type.

When the fatigue range was extended to the VHCF range ($N_f \ge 1.0\times10^7$), σ_f values were slightly lower than those in the HCF range, but was reversed having values of 795 MPa and 805 MPa for the shot-peened and unpeened specimen, respectively. The decrease of σ_f for shot-peened specimen was thought to be still mild, but definitely larger than that of unpeened one, which was quite different from the results by Trško et al. [33] who utilized high strength and low alloy steel 50CrMo4 under the ultrasonic fatigue tests at a frequency of 20 kHz. Because allowable stress for engineering design and application of the present spring steel was 320 MPa (one-fifth of σ_u) assuming the safety factor of 5.0, the decreasing slope did not seem to be a dangerous situation for spring components during the service life. With removal of the surface dimples with the maximum depth of 7 m and thus decreasing the surface roughness shown in Secs. 3.1-3.3 to relax the stress concentration in the skin part, the reversed situation in the σ_f by shot-peening would be improved for assuring better life.

Table 6 shows the regression curves calculated according to the fatigue cycle ranges. The accuracy of linear regression is represented by the regression coefficient (R^2 = SSR/SST) where SSR and SST are the residual and total sum of squares, respectively. High R^2 value indicates a small deviation of test data from the regression curve. In the HCF range, the shot-peening caused an increase in the initial fatigue strength A as well as in slope B. Data deviations in the shot-peened specimens were much less. The results were consistent with those [7] obtained by different experiments using the uniaxial tension-compression loading. However, in the VHCF range, shot-peening brought about a significant increase in B, and its positive effect was hardly seen in improving the fatigue strength, while the shot-peening treatment suppressed very much the scattering of the strength data so that the expected fatigue life was much more reliable.

The actual stress distribution, according to the depths in the specimen, was calculated considering the surface roughness and compressive residual stress, which acted on the surface and interior of the shot-peened specimens. In Sec. 3.3, the stress concentration factor (K_{tn}) of the skin part was 1.8-2.1

Table 6. Regression curves of fatigue strength and the regression coefficient (R^2) for unpeened and shot-peened specimens according to cycle ranges. R^2 (= SSR/SST) represents the accuracy of linear regression, where SSR and SST are the residual and total sum of squares, respectively.

	Cycle range	Regression curve	R^2 (= SSR/SST)
Unpeened	~ 10^6	$\sigma_a = 1185 - 67.32 \log_{10} N_f$	0.714
	10^6~VHCF	$\sigma_a = 828.1 - 2.56 \log_{10} N_f$	0.400
Shot-peened	~ 10^6	$\sigma_a = 1385 - 100.1 \log_{10} N_f$	0.816
	10^6~VHCF	$\sigma_a = 890.6 - 11.38 \log_{10} N_f$	0.879

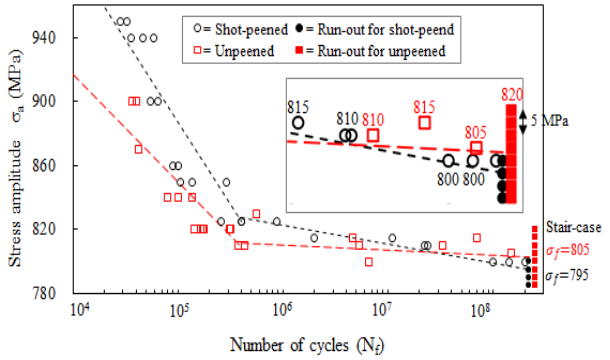

Fig. 7. Data points of the stress amplitudes (S) versus the number of cycles (N_f) for unpeened (□) and shot-peened (○) spring steel specimens. Solid marks indicate run-out data at the test end cycle of 2.5×10^8. The fatigue limit for each specimen type was determined using the stair-case method.

after shot-peening. The residual stress (σ_{rd}) and stress concentration factor (K_{tn}) were applied to calculate the actual stress (σ_A) on the skin part using equation

$$\sigma_A = K_{tn} \cdot (\sigma_0 + \sigma_{rd}) \quad (4)$$

where σ_0 is the nominal stress at the corresponding depth. The surface notch of the shot-peened specimen had various geometries of dimple depth (t) = 3-6 μm and radius (r) = 13-20 μm. Based on the surface profile geometry data, local stresses at the actual surface were estimated reflecting tensile σ_0, compressive σ_{rd}, and concentration K_{tn}. In a way similar to the previous studies [45-47], the lowest depth corresponding to no stress concentration was determined using the dimple depth and radius data. K_{tn} approached almost 1.0 in specimen depth larger than 55 μm. As illustrated in Fig. 8, K_{tn} was assumed to be 2.0 (Sec. 3.3) at the surface and set to converge to 1.0 at depths ≥ 55 μm. The tensile stress reduction, due to a significant increase in compressive residual stress in the skin part, was higher than the tensile stress increments due to stress concentration. Thus, the actual stress σ_A became lower than σ_0. The decrease of σ_A by shot-peening treatment led to an increase in nominal fatigue strength. However, in the VHCF range, although the nominal stress σ_0 got lower than the fatigue limit σ_f, the actual stress σ_A of the surface was higher

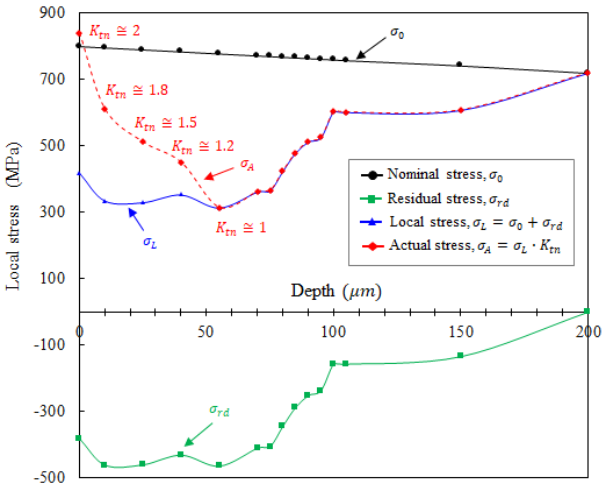

Fig. 8. Distributions of nominal (σ_0), residual (σ_{rd}), local (σ_L), and actual (σ_A) stresses along the depth from the surface for shot-peened specimens. The actual stress (σ_A) calculation reflected the surface roughness and compressive residual stress, which acted on the surface as well as the interior of the shot-peened specimens. K_{tn} of the skin part due to shot-peening was 1.8-2.1. The lowest depth corresponding to no stress concentration (K_{tn} = 1) was calculated around 55 μm. K_{tn} was calculated 2.0 at the surface.

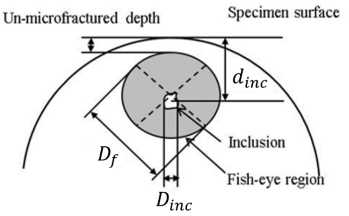

Fig. 9. Definitions of fracture surface geometrical parameter. This illustrates typical fracture pattern observed in the fracture surface of fatigued spring steel.

than σ_f, which caused the fatigue fracture, and thus a decrease in the nominal fatigue limit. In contrast, unpeened specimens had a low surface roughness, and scarcely generated stress concentrations. Without defects or inclusions in the skin of unpeened specimens, fatigue failure hardly seemed to occur in the VHCF range even for high stress amplitude (σ_a) of 820 MPa, as shown in Fig. 7. In this state, the fatigue limit of unpeened specimens could be higher than that of shot-peened specimens.

3.6 Shot-peening effects on the VHCF fracture behavior

Most fatigue fractures in the VHCF range originated from the inclusion of small oxide particles or grain boundaries of the metal poly-crystals, and formed a dark zone called the "fish-eye region" [6, 13, 18, 19] on the fracture surface, as illustrated in Fig. 9. Such failure mode was often observed for low stress amplitude and HCF range of hardened steels. The shot-peened specimens showed obviously longer fatigue life than unpeened specimen below $N_f = 3.0 \times 10^7$ cycles, as shown in

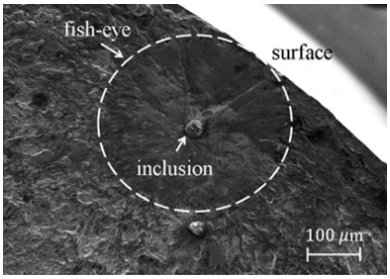

Fig. 10. SEM observation of the fracture surface of an unpeened specimen (σ_f = 810 MPa, N_f = 3.3×10^7 cycles, D_f = 300 μm, dinc = 178 μm). This photograph was taken for the largest fish-eye region detected near the specimen surface among unpeened specimens tested in the VHCF range.

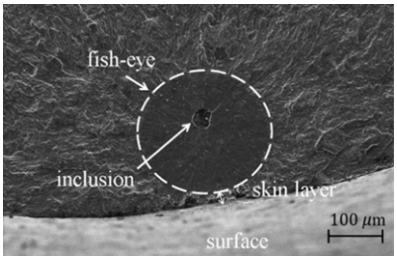

Fig. 11. SEM observation of the fracture surface of a shot-peened specimen (σ_f = 800 MPa, N_f = 1.4×10^8 cycles, D_f = 229 μm, dinc = 156 μm). This was taken for the largest fish-eye region detected near the specimen surface among shot-peened specimens tested in the VHCF range.

Fig. 7. In a range larger than N_f = 3.0 × 10^7 cycles, the fatigue strength was dependent on the position and size of the inclusion. Shot-peening was rather ineffective in VHCF behavior, which was dominated by the internal fracture characteristics as follows.

Through the SEM examination, the fish-eye regions in the shot-peened and unpeened specimens were also found in the VHCF range. Regardless of specimen types, the size of the inclusion was approximately 30 to 35 μm almost similar for all fractured specimens. However, the fish-eye regions had variations in size and shape. It is to be noted that such variations of the fish-eye regions may have been affected by the compressive residual stress distribution and skin layer change due to the shot-peening.

Figs. 10 and 11 show the largest fish-eye regions among those observed near the specimen surface in the VHCF range through this study for unpeened and shot-peened specimens, respectively. The largest size of fish-eye may indicate the longest duration of microfracturing process initiated at the corresponding inclusion. For the unpeened specimen of Fig. 10, the diameter of fish-eye (D_f) was around 300 μm, and the depth of inclusion from the surface (dinc) was 178 μm. D_f for the shot-peened specimen (Fig. 11) was 229 μm, and dinc was 156 μm. The value of dinc at the fish-eye center of unpeened specimen was much deeper than that in the shot-peened specimen, while the maximum D_f of unpeened specimen was much larger. For unpeened specimen, the skin crack initiated with a fish-eye pattern caused a more rough and bumpy fracture than that in the shot-peened specimen.

Table 7. Fatigue properties of the fish-eye fracture before and after shot-peening. The data are obtained from Figs. 10 and 11 which correspond to the largest fish-eye region detected for unpeened and shot-peened specimens tested in the VHCF range, respectively.

Specimen	Unpeened Fig. 10	Shot-peened Fig. 11
Stress amplitude at surface (MPa)	810	800
Inclusion depth (μm)	178	156
Actual stress at inclusion (MPa)	737.9	737.6
Number of cycles (N_f)	3.3 × 10^7	1.4 × 10^8
Fish-eye's radius (D_f/2, μm)	150	114.5
Crack growth per cycle (D_f/2N_f, μm)	4.54 ×10^{-7}	0.82 × 10^{-7}

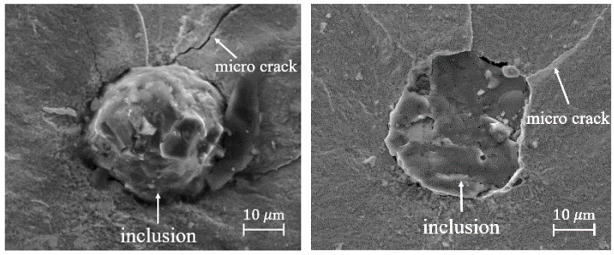

(a) (b)

Fig. 12. SEM observation of inclusions at the fracture initiation site in Figs. 10 and 11: (a) unpeened (dinc = 33 μm); (b) shot-peened specimen (dinc = 34 μm).

Fig. 12 shows the highly magnified photographs around the inclusions corresponding to the fish-eye initiation site. The size of inclusion for unpeened specimens (Fig. 12(a)) was little different from that for the shot-peened specimen (Fig. 12(b)). The EDX analysis showed that the inclusion in an unpeened specimen was a non-metallic compound composed of C, S, Ca and Al oxides. The inclusions must have different modulus from the steel matrix, which induced quite large stress concentration behaviors at the inclusion site.

Although there were shown different stress amplitudes at the surface for unpeened and shot-peened specimens, it is to be noted in Table 7 measured in Figs. 10 and 11 corresponding to the largest fish-eye sizes formed in the VHCF tests that the actual local stresses calculated around the inclusions using the stressconcentration effect [48] were nearly the same (about 737.6~737.9 MPa) for both specimens. However, the fatigue life for the shot-peened specimen was four times longer, and the depth of inclusion (dinc) for fish-eye initiation was more shallow than the unpeened specimen. Most fish-eye fractures arose at sites (dinc > 100 μm) deeper than the compressive residual stress zone, which did not prevent the creation itself of

the fish-eye. Therefore the fatigue strength improvement in the VHCF range could be scarcely expected as a result of the shot-peening treatment.

On the other hand the fish-eye region in the shot-peened specimen in Fig. 10 was larger than the unpeened specimen, while the crack growth per cycle largely decreased to approximately 18 % because the micro-cracking toward the surface was hindered by the high compressive residual stresses dominating in the skin part. It is ascertained that the compressive stress suppressed the microcrack growth, leading to the slow growth of the fish-eye in the skin part. Thus the fish-eye region for shot-peened specimens was shaped into a more elliptical form. The depth of the un-microfractured layer (Fig. 9) was around 20 μm which corresponded to the location of the maximum compressive residual stress shown in Fig. 2, which was consistent with the result of the previous study [27].

4. Conclusions

The rotary bending fatigue test was carried out over the span of high-cycle and very high cycle life using unpeened and shot-peened spring steels. The shot-peening of about 200 % coverage formed a large amount of compressive residual stress in the skin part. Further, most of the subsurface-originated fracture and scattering of the fatigue test data were definitely suppressed, and the fatigue strength in the cycle range below 3.0×10^7 cycles was considerably improved. The shot-peening effect on suppressing the subsurface cracks was clearly confirmed in improving fatigue life in the HCF range. On the basis of Goodman equation presupposing a uniaxial test specimen, the conventional fatigue limits at $N_f = 1.0\times10^7$ were expected to be 56.4 % and 66.8 % of the tensile strength for unpeened and shot peened specimens, respectively, which were considerably larger than those measured experimentally by the staircase method. The difference in strength could be caused by specimen types of uniaxial and rotary bending tests for unpeened specimens, while it for shot-peened specimens originated from residual stress distribution characteristics and microstructural changes in addition to specimen type.

When the fatigue cycle was extended to the VHCF range ($N_f \geq 1.0\times10^7$), the fatigue limit values were slightly lower than those in the HCF range, but was reversed having values of 795 MPa and 805 MPa for the shot-peened and unpeened specimen, respectively. The decrease of the fatigue limit value for shot-peened specimen was definitely larger than that of unpeened one. Although the decreasing fatigue limit did not represent a dangerous situation for spring components during the service life, the reversed situation in the fatigue limit by shot-peening should be improved for assuring better reliability and longer service life in actual application to spring components through removal of the surface dimples, minimizing the surface roughness, and thus relaxing the stress concentration in the skin part.

Regardless of the shot-peening treatment, most fatigue fractures occurred from fish-eye fractures, which arose at sites deeper than the compressive residual stress zone up to around 100 μm in depth. The compressive residual stress zone created by shot-peening treatment did not prevent the initiation itself of the fish-eye fractures. The fatigue strength improvement in the VHCF range could scarcely be expected using the shot-peening treatment.

Surface polishing needs to be performed for up to 7 μm in depth underneath the surface to remove various peening-defects and roughness within the limit that the maximum compressive stress zone in the skin part should be maintained. Through this process a positive effect in the fatigue strength in the VHCF range can be expected which remains for a further study.

Acknowledgments

This research was supported by Basic Science Research Program through the National Research Foundation of Korea (NRF) funded by the Ministry of Science, ICT and Future Planning (NRF-2019R1A2C1002193). Thanks to the Korea Atomic Energy Research Institute (KAERI) for authorizing the use of XRD.

Nomenclature

R	: Stress ratio
σ	: Nominal stress of the gauge portion
M	: The maximum bending moment
c	: Distance from the neutral axis to a designated height
I	: Geometrical moment of inertia at the gage part
α	: Stress concentration factor
P	: Load
m	: Fixed test span
d	: Gage part cross-section diameter
R_a	: Average roughness
R_q	: Root mean square
K_{tn}	: Stress concentration factor
σ_0	: Nominal stress
σ_a	: Stress amplitude
N_f	: Number of fatigue test cycles
A	: Y-intercept that indicates the initial fatigue strength
B	: Decreasing slope of fatigue strength as the life cycle increases
σ_f	: Fatigue limit
σ_u	: Tensile strength
σ_{f0}	: Fatigue limit of unpeened uniaxial specimen
σ_{u0}	: Tensile strength of unpeened uniaxial specimen
σ_m	: Mean stress
σ_{rd}	: The maximum residual stress
R^2	: Regression coefficient
SSR	: Residual sum of squares
SST	: Total sum of squares
σ_A	: Actual stress
σ_L	: Local stress
D_f	: Diameter of fish-eye

References

[1] B. Pyttel, D. Schwerdt and C. Berger, Very high cycle fatigue - is there a fatigue limit?, *International Journal of Fatigue*, 33 (2011) 49-58.

[2] K. Shiozawa and L. Lu, Very high cycle fatigue behavior of shot-peened high carbon chromium bearing steel, *Fatigue and Fracture of Engineering Materials & Structures*, 25 (8-9) (2002) 813-822.

[3] Y. Furuya, T. Abe and S. Matsuoka, 1010-cycle fatigue properties of 1800 MPa-class JIS-SUP7 spring steel, *Fatigue and Fracture of Engineering Materials & Structures*, 26 (2003) 641-645.

[4] T. Sakai, A. Nakagawa, N. Oguma, Y. Nakamura, A. Ueno, S. Kikuchi and A. Sakaida, A review on fatigue fracture modes of structural metallic materials in very high cycle regime, *International Journal of Fatigue*, 93 (2016) 339-351.

[5] H. Kim, G. Kim, W. Ji, Y. S. Lee, S. Jang and C. M. Shin, Random vibration fatigue analysis of a multi-material battery pack structure for an electric vehicle, *Functional Composites and Structures*, 3 (2021) 025006.

[6] C. Bathias and P. C. Paris, *Giga-cycle Fatigue in Mechanical Practice*, Marcel Dekker, New York (2005).

[7] B. Nie, Z. Zhang, Z. Zhao and Q. Zhong, Very high cycle fatigue behavior of shot-peened 3Cr13 high strength spring steel, *Materials & Design*, 50 (2013) 503-508.

[8] Y. Akiniwa, S. Stanzl-Tschegg, H. Mayer, M. Wakita and K. Tanaka, Fatigue strength of spring steel under axial and torsional loading in the very high cycle regime, *International Journal of Fatigue*, 30 (2008) 2057-2063.

[9] C. Berger and B. Kaiser, Results of very high cycle fatigue tests on helical compression springs, *International Journal of Fatigue*, 28 (11) (2006) 1658-1663.

[10] B. Pyttel, I. Brunner, B. Kaiser, C. Berger and M. Mahendran, Fatigue behavior of helical compression springs at a very high number of cycles - investigation of various influences, *International Journal of Fatigue*, 60 (2014) 101-109.

[11] T. Abe, Y. Furuya and S. Matsuoka, Gigacycle fatigue properties of 1800 MPa class spring steels, *Fatigue and Fracture of Engineering Materials & Structures*, 27 (2) (2004) 159-167.

[12] Y. Furuya and T. Abe, Effect of mean stress on fatigue properties of 1800 MPa-class spring steels, *Materials & Design*, 32 (2011) 1101-1107.

[13] Y. Murakami, *Metal Fatigue: Effects of Small Defects and Nonmetallic Inclusions*, 1st Ed., Elsevier, Oxford (2002).

[14] Y. Murakami, S. Kodama and S. Konuma, Quantitative evaluation of effects of non-metallic inclusions on fatigue strength of high strength steels, *International Journal of Fatigue*, 11 (5) (1989) 291-298.

[15] S. Nishijima and K. Kanazawa, Stepwise S-N curve and fish-eye failure in gigacycle fatigue, *Fatigue and Fracture of Engineering Materials & Structures*, 50 (7) (1997) 601-607.

[16] R. Yakura, M. Matsuda, T. Sakai and A. Ueno, Effect of inclusion size on fatigue properties in very high cycle region of low alloy steel used for solid type crankshaft, *Kobelco Technology Review,* 35 (2017) 7-13.

[17] S. T. Tu and X. C. Zhang, Fatigue crack initiation mechanisms, *Reference Module in Materials Science and Materials Engineering* (2016).

[18] K. Shiozawa, L. Lu and S. Ishihara, S-N curve characteristics and subsurface crack initiation behavior in ultra-long life fatigue of a high carbon-chromium bearing steel, *Fatigue and Fracture of Engineering Materials & Structures*, 24 (12) (2001) 781-790.

[19] K. Shiozawa, Y. Morii, S. Nishino and L. Lu, Subsurface crack initiation and propagation mechanism in high-strength steel in a very high cycle fatigue regime, *International Journal of Fatigue*, 28 (11) (2006) 1521-1532.

[20] M. Marini, F. Piona, V. Fontanari, M. Bandini and M. Benedetti, A new challenge in the DEM/FEM simulation of the shot peening process: the residual stress field at a sharp edge, *International Journal of Mechanical Science*, 169 (2020) 105327.

[21] J. Wu, H. Liu, P. Wei, Q. Lin and S. Zhou, Effect of shot peening coverage on residual stress and surface roughness of 18CrNiMo7-6 steel, *International Journal of Mechanical Science*, 183 (2020) 105785.

[22] K. Sherafatnia, G. H. Farrahi and A. H. Mahmoudi, Effect of initial surface treatment on shot peening residual stress field: analytical approach with experimental verification, *International Journal of Mechanical Science*, 137 (2018) 171-181.

[23] C. Wang, L. Wang, X. Wang and Y. Xu, Numerical study of grain refinement induced by severe shot peening, *International Journal of Mechanical Science*, 146-147 (2018) 280-294.

[24] M. Korzynski, Predicting the height of uneven surface after ball-peening machining, *International Journal of Mechanical Science*, 150 (2019) 617-624.

[25] X. Xiao, X. Tong, Y. Liu, R. Zhao, G. Gao and Y. Li, Prediction of shot peen forming effects with single and repeated impacts, *International Journal of Mechanical Science*, 137 (2018) 182-194.

[26] J. K. Xenonphon, Shot peening viable method to extending component life, *SAE Technical Paper Series 891932* (1989) 1-8.

[27] S. J. Yoon, J. H. Park and N. S. Choi, Fatigue life analysis of shot-peened bearing steel, *Journal of Mechanical Science and Technology*, 26 (6) (2012) 1747-1754.

[28] S. C. Chung and S. D. Back, Effect of shot peening on fatigue properties in spring steel, *Transaction of the Korean Society of Mechanical Engineers A*, 22 (6) (1998) 1009-1015.

[29] T. S. Lee, J. H. Jang, C. M. Suh, J. H. Kim and S. C. Kim, Fatigue characteristics of bearing steel in giga cycles, *Transaction of the Korean Society of Mechanical Engineers A*, 10 (2007) 165-169.

[30] G. Fargas, J. J. Roa and A. Mateo, Effect of peening on metastable austenitic stainless steels, *Materials Science and Engineering A*, 641 (2015) 290-296.

[31] J. K. Li, M. Yao, D. Wang and R. Wang, An analysis of stress concentrations caused by shot peening and its application in predicting fatigue strength, *Fatigue and Fracture of Engineering Materials & Structures*, 15 (12) (1992) 1271-1279.

[32] S. Bagherifard, I. Fernandez-Pariente, R. Ghelichi and M. Guagliano, Fatigue behavior of notched steel specimens with nanocrystallized surface obtained by severe shot peening, *Materials & Design*, 45 (2013) 497-503.
[33] L. Trško, O. Bokůvka, F. Nový and M. Guagliano, Effect of severe shot peening on ultra-high-cycle fatigue of a low-alloy steel, *Materials & Design*, 57 (2014) 103-113.
[34] M, Benedetti, V. Fontanari, M. Bandini and E. Savio, High- and very high-cycle plain fatigue resistance of shot peened high-strength aluminum alloys: the role of surface morphology, *International Journal of Fatigue*, 70 (2015) 451-462.
[35] KS B ISO 1143:2003, *Metals - Rotating Bar Bending Fatigue Testing*, Korean Standard Association, Republic of Korea (2003).
[36] M. G. Moore and W. P. Evans, Correction for stress layers in X-ray diffraction residual stress analysis, *SAE Transaction*, 64 (1) (1958) 340-345.
[37] A. Bahri, M. Ellouz , M. Klöcker, T. Kordisch and K. Elleuch, Brinell indentation behavior of the stainless steel X2CrNi18-9: modeling and experiments, *International Journal of Mechanical Science*, 163 (2019) 105142.
[38] Z. F. Zhang and Z. G. Wang, Grain boundary effects on cyclic deformation and fatigue damage, *Progress in Materials Science*, 53 (7) (2008) 1025-1099.
[39] F. Morel, A. Morel and Y. Nadot, Comparison between defects and micro-notches in multiaxial fatigue - the size effect and the gradient effect, *International Journal of Fatigue*, 31 (2) (2009) 263-275.
[40] Y. Murakami and M. Endo, Effects of defects, inclusions and inhomogeneities on fatigue strength, *International Journal of Fatigue*, 16 (3) (1994) 163-182.
[41] Y. Murakami, Effects of small defects and nonmetallic inclusions on the fatigue strength of metals, *JSME International Journal*, 32 (2) (1989) 167-180.
[42] Y. Murakami and T. Endo, Effects of small defects on fatigue strength of metals, *International Journal of Fatigue*, 1 (1980) 23-30.
[43] W. D. Pilkey and D. F. Pilkey, *Peterson's Stress Concentration Factors*, 3rd Ed., John Wiley & Sons Publishing Company, New Jersey (2008).
[44] H. Tada, P. C. Paris and G. R. Irwin, *The Stress Analysis of Cracks Handbook*, 3rd Ed., ASME Press, New York (2000).
[45] Z. Xu, W. Wen and T. Zhai, Effects of pore position in depth on stress/strain concentration and fatigue crack initiation, *Metallurgy and Materials Transaction A*, 43 (8) (2011) 2763-2770.
[46] F. N. Jespersen, J. H. Hattel and M. A. J. Somers, Modelling the evolution of composition-and stress-depth profiles in austenitic stainless steels during low-temperature nitriding, *Modelling and Simulation of Materials Science and Engineering*, 24 (2) (2016) 025003.
[47] T. Yasuoka, Y. Mizutani and A. Todoroki, The correction of stress intensity factor for crack growth evaluation under steep residual stress distribution and steep yield strength distribution, *Materials and Fabrication*, 6A (2013).
[48] A. Nakagawa, T. Sakai, D. G. Harlow, N. Oguma, Y. Nakamura, A. Ueno and A. Sakaida, A probabilistic model on crack initiation modes of metallic materials in very high cycle fatigue, *Procedia Structural Integrity*, 2 (2016) 1199-1206.

NohJun Myung received his Doctor's degree from the Department of Mechanical Engineering, Hanyang University, Korea, in 2020. His research interests involve fatigue life analysis and material design.

Liang Wang received his Master's degree from the Department of Mechanical Design Engineering, Hanyang University, Korea, in 2018. His research interests involve composite analysis and material design.

Nak-Sam Choi is a Professor of Department of Mechanical Engineering, Hanyang University (ERICA), Korea. He received his B.S. in Mechanical Engineering from Seoul National University, Korea, his M.S. in Mechanical Engineering from KAIST, and Ph.D. in Composite Materials & Applied Mechanics from Kyushu University, Japan. His research interests include composites science, fatigue life and microstrain analysis, and nondestructive examination of advanced materials.